Surface & Coatings Technology 532 (2026) 133598

Contents lists available at ScienceDirect

Surface & Coatings Technology

journal homepage: www.elsevier.com/locate/surfcoat

Bilayer wear-resistant coating on Al 6061 fabricated by SiC nanofluid-enhanced WEDM: Role of pulse duration in structure and oil-free tribology

Cuixia Guo [a,b,*], Gui He [a,b], Jianping Zhang [a,b], Xinjun Zhou [a,b], Shixue Zhang [a], Zhangyong Wu [c]

[a] Faculty of Mechanical Engineering, Sichuan University of Science & Engineering, Zigong, 643000, China
[b] Material Corrosion and Protection Key Laboratory of Sichuan Province, Zigong, 643000, China
[c] Faculty of Mechanical and Electrical Engineering, Kunming University of Science and Technology, Kunming, 650500, China

ARTICLE INFO

Keywords:
Emulsion-based SiC nanofluid
Bilayer coating
Pulse duration
In-situ surface modification
Oil-free tribology
Wear resistance

ABSTRACT

To meet the wear resistance requirements of lightweight aluminum alloys in aerospace applications, this study proposes an in-situ surface modification method: fabricating a bilayer wear-resistant coating on Al 6061 via high-speed wire electrical discharge machining (HS-WEDM) using an emulsion-based SiC nanofluid dielectric (*E*-SiC-NFD). This work focuses on the regulatory role of pulse duration-related effects on the in-situ formation, mechanical properties and oil-free tribological performance of the bilayer coating. The core findings and contributions of this work are as follows: (1) A heterogeneous bilayer coating consisting of a soft self-lubricating covering layer and a hard load-bearing recast layer is in-situ fabricated in one step, and the core Pinning-Locking interfacial strengthening mechanism between the two layers is systematically elucidated; (2) The regulatory law of pulse duration-related effects on the microstructure, thickness, microhardness and tribological properties of the bilayer coating is revealed, and the optimal process window for comprehensive performance is determined at the pulse duration of 6 μs; (3) The decoupling mechanism of friction reduction and wear resistance is clarified, which demonstrates that the lowest coefficient of friction (COF) and the longest wear life are governed by two independent competing mechanisms: the COF is dominated by the formation of graphite-like self-lubricating phases, while the wear life is determined by the mechanical strength of the coating and interlayer interfacial integrity. At the optimal pulse duration of 6 μs, the coating achieves the longest wear life of 66 min with a stable COF of 0.189; extending the pulse duration to 12 μs obtains the lowest COF of 0.143, but the wear life is significantly shortened to 27 min. This work realizes the integration of precision forming and in-situ surface strengthening of aluminum alloys, and provides an efficient, low-cost integrated process for the wear-resistant modification of lightweight aluminum alloys.

1. Introduction

Aluminum alloys are ideal lightweight structural materials for automotive and aerospace applications, owing to their low density (~2.7 g/cm^3), high specific strength, and excellent corrosion resistance [1,2]. However, their inherent poor tribological properties, characterized by low surface hardness and low seizure load, severely limit long-term service performance in moving components under harsh working conditions. Accordingly, surface modification is an indispensable procedure to meet the stringent wear resistance requirements of industrial applications [1,3].

Conventional surface modification technologies, including thermal spraying [4], laser cladding [5], electroplating [6], physical vapor deposition (PVD) [7], and micro-arc oxidation [8], have been widely employed to enhance the wear resistance of aluminum alloys. Nevertheless, these techniques face inherent technical and economic limitations in industrial implementation: thermal spraying requires specialized equipment and strict environmental controls, electroplating generates toxic effluents with severe environmental hazards, PVD relies on costly high-vacuum systems, and micro-arc oxidation suffers from excessive energy consumption. More importantly, these conventional technologies generally require multiple independent sequential procedures, and exhibit poor adaptability to batch fabrication of aluminum alloy components with complex cavities and thin-walled structures.

* Corresponding author at: Faculty of Mechanical Engineering, Sichuan University of Science & Engineering, Zigong, 643000, China.
E-mail address: gcx@suse.edu.cn (C. Guo).

https://doi.org/10.1016/j.surfcoat.2026.133598
Received 23 March 2026; Received in revised form 6 May 2026; Accepted 15 May 2026
Available online 20 May 2026

These barriers drive an urgent demand for a cost-effective, integrated machining-modification method for aluminum alloys.

As a non-contact precision machining technology, high-speed wire electrical discharge machining (HS-WEDM) exhibits unique advantages including no macroscopic cutting force, negligible tool wear, and exceptional adaptability to complex geometric components, and has become one of the core mainstream processes for manufacturing high-precision aluminum alloy parts [9–11]. However, the non-equilibrium thermodynamic process of instantaneous high-temperature melting and rapid solidification during HS-WEDM inevitably introduces inherent defects such as micro-cracks and softened layers on the machined surface, which significantly deteriorate the service performance and fatigue life of the components [12,13]. In this context, powder-mixed electrical discharge machining (PMEDM) has emerged as a promising surface modification strategy [14,15]. By introducing micro/nano-scale powders into the dielectric fluid, the transient high-temperature plasma during discharge triggers in-situ metallurgical reactions on the workpiece surface, enabling one-step fabrication of a functional modified layer without additional pre-treatment or post-processing [16–21]. Among various powder additives, silicon carbide (SiC) has been extensively investigated in PMEDM due to its ultra-high hardness, excellent wear resistance, and high-temperature stability [22]. For instance, Mughal et al. [23] reported that SiC powder addition significantly enhanced the surface microhardness of Ti6Al4V alloy from 320 HV to 727 HV via PMEDM. Nevertheless, most existing studies on SiC powder-mixed EDM have predominantly focused on mitigating defects of a single monolithic recast layer and improving its hardness, with very limited optimization of the friction reduction performance of the machined surface, failing to achieve synergistic optimization of low friction and high wear resistance [24,25].

Nanofluids have emerged as an innovative dielectric for EDM, exhibiting superior thermal conductivity, electric field responsiveness, and sedimentation stability compared to conventional powder-mixed dielectric fluids [26–30]. In previous work [31], the authors first reported that an emulsion-based SiC nanofluid dielectric (*E*-SiC-NFD) can be applied for HS-WEDM surface modification of Al 6061 alloy, and that a bilayer heterogeneous coating can be in-situ formed on the alloy surface, which exhibits significantly better tribological performance than the monolayer recast layer fabricated by conventional processes. However, the in-situ formation mechanism of this bilayer coating, the regulatory effect of key process parameters on coating structure and tribological performance, as well as the underlying structure-performance correlation, remain unclear, which restricts the optimization and industrial application of this technology.

Against this background, this work systematically conducts an in-depth investigation of in-situ surface modification of Al 6061 alloy via *E*-SiC-NFD-assisted HS-WEDM, with a focus on the regulatory mechanism of pulse duration-related effects on the microstructure, mechanical properties, and oil-free tribological performance of the bilayer coating. The core contributions of this work are as follows: (1) A heterogeneous bilayer coating with a soft self-lubricating covering layer and a hard load-bearing recast layer is in-situ fabricated on Al 6061 via *E*-SiC-NFD-assisted HS-WEDM, and the Pinning-Locking interfacial strengthening mechanism that dominates the interlayer bonding performance is systematically elucidated; (2) The non-monotonic evolution law of the coating's microstructure, mechanical properties and tribological performance regulated by pulse duration-related effects is revealed, and the optimal process window for the comprehensive performance of the bilayer coating is determined; (3) The decoupling mechanism of friction reduction and wear resistance of the bilayer coating is clarified, which demonstrates that the lowest COF and the longest wear life are governed by distinct competing mechanisms, providing a flexible design principle for the performance tailoring of solid lubricating wear-resistant coatings.

2. Preparation of emulsion-based SiC nanofluid

The emulsion-based SiC nanofluid dielectric (*E*-SiC-NFD, 3 g/L) was prepared via a two-step method following the protocol reported in Ref. [32]. SiC nanoparticles (average particle size of 50 nm, purity ≥99.9%, bulk density of 3160 kg/m^3) were supplied by Shanghai Chaowei Nanotechnology Co., Ltd. (Shanghai, China); sodium dodecyl benzene sulfonate (SDBS, analytical grade (AR), purity ≥99.0%) was obtained from Shanghai Aladdin Biochemical Technology Co., Ltd. (Shanghai, China); and JR3A special emulsion cream for HS-WEDM was purchased from Jiarun Wire Cutting Fluid Manufacturer (Zhuji, Zhejiang, China). Transmission electron microscopy (TEM, Fig. 1(a)) of the as-received SiC nanoparticles revealed that the primary particles are nearly spherical, and that slight agglomeration can be effectively eliminated via dispersion with SDBS.

During preparation, SiC nanoparticles and SDBS were uniformly dispersed into an oil-in-water (O/W) emulsion (Fig. 1(b)), which was formulated by mixing JR3A commercial emulsion cream with distilled water at a mass ratio of 1:50. This ratio was adjusted from the 1:100 ratio used in Ref. [32], which was optimized for high-precision multi-cut HS-WEDM to ensure machining accuracy and surface quality. In this work, however, the adopted 1:50 ratio was optimized via systematic preliminary experiments to meet the requirements of in-situ surface modification, achieving two synergistic objectives: (1) providing a sufficient carbon source for the in-situ formation of graphite-like self-lubricating phases during discharge, and (2) avoiding discharge instability caused by reduced dielectric breakdown strength, which would result from excessively high oil content. The as-prepared nanofluid exhibited good colloidal stability (physical image shown in Fig. 1(c)), and consisted of SiC nanoparticles, mineral oil droplets, and SDBS; its microscopic composition is schematically illustrated in Fig. 1(d). The zeta potential (−36 m*V*) and electrophoretic mobility (4.39×10^{-8} $m^2 \cdot V^{-1} \cdot s^{-1}$) of the nanofluid were measured via the moving boundary method, confirming excellent colloidal stability derived from the synergistic effect between the SiC nanoparticles and the SDBS surfactant.

3. Experimental design and methods

3.1. Machined materials

Al 6061 alloy was selected as the substrate material due to its high specific strength, low density and good corrosion resistance. Its inherently poor tribological performance is the main limitation for engineering applications, which motivates this surface modification work. The alloy was supplied by Hongnian Metal Materials Co., Ltd., China, and its chemical composition is given in Table 1.

As a baseline reference, the Al 6061 substrate exhibits a microhardness of ~95 HV under the same indentation conditions as the coated samples. Under identical dry sliding conditions, its average friction coefficient is 0.621, as reported in our previous study [31]. These inherent properties of the uncoated substrate provide a reliable benchmark for evaluating the tribological performance of the prepared bilayer coating.

3.2. Experimental setup of HS-WEDM

Machining experiments were performed on a DKN280BZ HS-WEDM system (Sichuan Shengyang CNC Machinery Co., Ltd., Zigong, China). For consistent definition and subsequent comparative analysis, two types of specimens were classified in this work as follows: (1) **Bilayer coating specimen**: The primary research object of this study, an in-situ bilayer composite coating fabricated via emulsion-based SiC nanofluid dielectric (*E*-SiC-NFD)-assisted HS-WEDM, consisting of an upper soft self-lubricating covering layer and a lower hard load-bearing recast layer; (2) **Inner recast layer specimen** (control group): The control sample fabricated with exactly the same HS-WEDM processing parameters as the corresponding bilayer coating experimental group. Only the

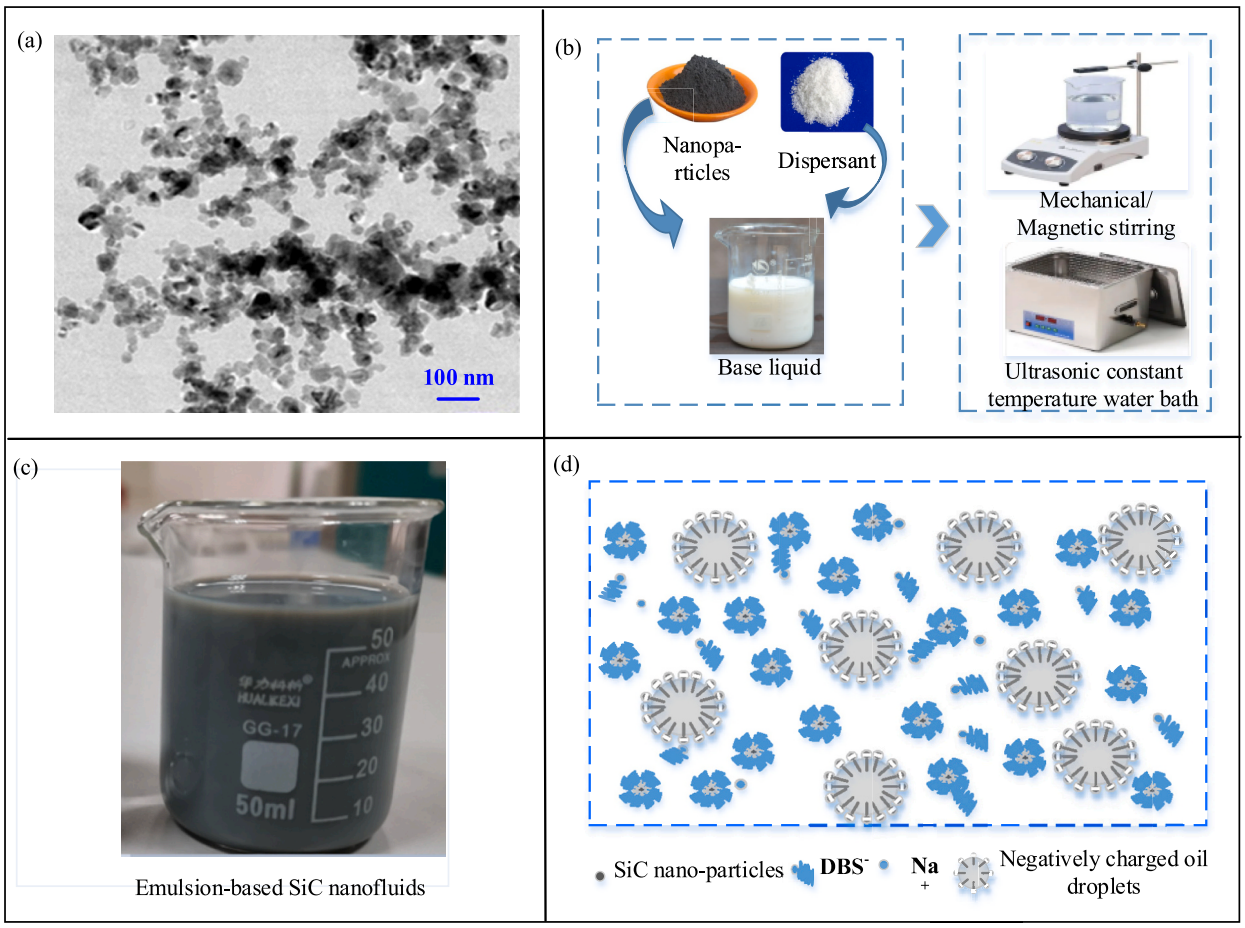

Fig. 1. Characteristics of emulsion-based SiC nanofluids: (a) TEM image of SiC nanoparticles; (b) Preparation process flow; (c) Physical photograph; (d) Schematic diagram of composition and microstructure.

Table 1
Chemical composition of the Al 6061 alloy (wt%).

Elements	Mg	Mn	Si	Cu	Zn	Fe	Cr	Ti	Al
wt%	0.8–1.2	0.15	0.4–0.8	0.15–0.4	0.25	0.7	0.04–0.35	0.15	Bal.

upper soft covering layer was completely removed from the machined surface via non-destructive toothpaste slurry scrubbing, with the hard recast layer formed during HS-WEDM retained exclusively.

3.3. Experimental design

Pulse duration is the core controllable process parameter in HS-WEDM, as its variation simultaneously triggers a series of coupled physical and chemical changes in the discharge gap, including single-pulse discharge energy, electrophoretic migration time window, molten pool thermal behavior, dielectric flow field state, and local concentration distribution of nanoparticles. These coupled changes are uniformly defined as pulse duration-related effects in this work, which dominate the electrophoretic migration of charged species and the in-situ formation of the bilayer coating. Hence, pulse duration was selected as the single variable in this experiment, with all other process parameters kept constant. The detailed experimental design is shown in Table 2.

3.4. Characterization and testing methods

3.4.1. Microstructure, elemental distribution and coating thickness

Microstructure, surface and cross-sectional morphologies were observed using a scanning electron microscope (SEM, TESCAN VEGA

Table 2
Experimental design of HS-WEDM process parameters with varied pulse duration.

Samples number	Processing	dielectric	Pulse Duration (μs)	Pulse interval (μs)	Power tube (number)	Pulse voltage (V)	Wire speed (m/s)
	Main cut	Emulsion	6	7	3	100	15
S1	Trim cut	*E*-SiC-NFD	2	12	1	50	3
S2			4	12	1	50	3
S3			6	12	1	50	3
S4			10	12	1	50	3
S5			12	12	1	50	3

3SBU, Czech Republic) equipped with an energy-dispersive X-ray spectrometer (EDS). Elemental mapping and line scan analyses were performed to characterize the distribution of Al, C, O, and Si across the coating cross-section.

The thicknesses of the bilayer coating and the inner recast layer (for the sample fabricated at 6 μs pulse duration) were measured from cross-sectional SEM images using Image J software. For each process parameter, measurements were taken at no fewer than 10 random positions on each of 3 parallel samples, and the results were reported as mean ± standard deviation (SD).

3.4.2. Thickness measurement of the soft covering layer

The thickness of the outer soft covering layer was measured using a TT230PLUS digital coating thickness gauge (Beijing Time Hengyu Technology Co., Ltd., China) based on the eddy current method. For each sample, 15 random test points were selected across the entire machined surface, and 3 parallel samples were tested for each pulse duration parameter. The final thickness was presented as mean ± SD.

3.4.3. Phase composition and chemical structure

Phase composition was identified by X-ray diffraction (XRD, Bruker D8 Advance, Germany) with Cu Kα radiation (λ = 0.15406 nm) at 40 k*V* and 40 mA. Data were collected over a 2θ range of 10°-90° at a scanning speed of 5°/min. To identify the phase constituents of the soft covering layer, powder scraped from the coating surface was also tested.

Chemical structure and self-lubricating phases were analyzed using a Raman spectrometer (DXR3, Thermo Fisher Scientific, USA) with a 532 nm laser, over a wavenumber range of 100–4000 cm^{-1}.

3.4.4. Microhardness and interfacial bonding strength

Vickers microhardness was measured using an HV-1000 microhardness tester under a static load of 50 g (0.49 N) with a dwell time of 10 s. A low indentation load was chosen specifically to avoid substrate influence. The indentation depth was recorded for each measurement to confirm that the hardness values reflected the intrinsic mechanical properties of individual layers, rather than the underlying substrate. For each layer of the coating, 5 random indentations were made on each sample, with 3 parallel samples tested per parameter, and the results were reported as mean ± SD.

Interfacial bonding strength was evaluated using a scratch tester (Anton Paar RST^3, Switzerland) equipped with a Rockwell diamond indenter (radius 200 μm). Progressive load tests were performed from 1 N to 20 N at a loading rate of 20 N/min over a 5 mm scan length. Critical loads for crack initiation (Lc1) and complete delamination (Lc2) were determined from the scratch morphology and synchronous friction force signal. For each sample, 3 parallel scratch tests were conducted, and the critical load values were presented as mean ± SD.

The control coating was fabricated with pure emulsion under the same process parameters as the optimal 6 μs bilayer coating sample, with only the dielectric changed, to ensure the single variable of the control experiment.

3.4.5. Tribological testing and definition of wear life

Tribological tests were carried out on an MFT-EC4000 reciprocating ball-on-flat tribometer under dry sliding conditions. A silicon nitride (Si_3N_4) ball (diameter 6 mm) was used as the counterpart. Test parameters: normal load 5 N, reciprocating frequency 1 Hz, stroke length 5 mm. The coefficient of friction (COF) was recorded continuously and plotted against sliding time.

In this work, wear life is defined as the sliding duration at which the coefficient of friction (COF) first exceeds 0.4. This threshold is established based on systematic pre-experimental observations: when the bilayer coating remains structurally intact, the steady-state COF maintains a stable range of 0.2–0.35; once the coating is fully worn through and direct contact with the Al alloy matrix occurs, the COF exhibits an irreversible sharp increase to 0.5–0.7. The value of 0.4 corresponds exactly to the critical transition point between intact service and complete coating failure.

The validity of this criterion is quantitatively verified via multi-scale characterization (Fig. 2). Cross-sectional profiling of the wear scar (Fig. 2(a)) shows that the maximum wear depth reaches ~22 μm at the failure threshold, which exceeds the total thickness of the pristine bilayer coating (20.8 μm, Fig. 2(c)), confirming that the entire protective bilayer is fully worn through at this point.

Wear morphology and profiles were analyzed using SEM, a 3D optical microscope (LY-WN-YH1000), and a SJ410 surface profilometer. All tribological tests were repeated at least three times to ensure statistical reliability. Data are presented as mean ± SD. One-way analysis of variance (ANOVA) was performed, with statistical significance accepted at $p < 0.05$.

4. Experimental results and discussion

4.1. Microstructure and composition of the bilayer coating

Microstructure, elemental distribution, phase composition, and basic mechanical properties of the bilayer coating in-situ synthesized on Al 6061 via *E*-SiC-NFD-assisted HS-WEDM were systematically characterized to verify its heterogeneous architecture and provide fundamental support for subsequent property analysis and mechanism clarification.

4.1.1. Surface and cross-sectional morphology

Surface and cross-sectional morphologies of the bilayer coating and inner recast layer (as defined in Section 3.2) were characterized by SEM and EDS, as presented in Fig. 3. The as-prepared surface with an intact bilayer coating exhibits a uniform grayish-black appearance without noticeable macroscopic defects (Fig. 3(a)), and displays a typical honeycomb-like micro-morphology derived from electrical discharge melting and rapid solidification (Fig. 3(b)). After selective removal of the upper soft covering layer using toothpaste slurry scrubbing, the underlying subsurface shows a smooth gray appearance with no observable mechanical damage (Fig. 3(d)), verifying the non-destructive nature of the adopted exfoliation method.

High-magnification SEM observations reveal that the exposed recast layer possesses characteristic microstructural features induced by spark discharge, including numerous discharge craters and solidified splashes (Fig. 3(e)). The electro-eroded particles are uniformly embedded in the inner recast layer without severe agglomeration. EDS point analysis (Table 3, position 0#) confirms significant enrichment of Si and C originating from SiC nanoparticles in the *E*-SiC-NFD dielectric. These in-situ embedded hard ceramic particles effectively impede grain boundary migration and dislocation motion during rapid solidification, thereby exerting a pronounced dispersion-strengthening effect on the recast layer.

Cross-sectional SEM characterization (Fig. 3(c, f)) clearly reveals a distinct heterogeneous bilayer architecture on Sample S3, fabricated at a pulse duration of 6 μs (the optimal process window): the upper soft covering layer with an average thickness of approximately 20.25 μm and a lower dense hard recast layer with an average thickness of approximately 10.7 μm. No obvious cracks, pores, or interfacial delamination were observed at the coating/substrate interface, confirming the formation of a robust metallurgical bonding between the recast layer and the Al 6061 substrate.

Overall, morphological results confirm that the *E*-SiC-NFD-assisted HS-WEDM process enables the one-step in-situ fabrication of a well-defined heterogeneous bilayer coating on the Al alloy surface, which is fundamentally different from the single homogeneous recast layer produced by conventional powder-mixed EDM. This unique bilayer structure provides the essential structural basis for the synergistic combination of low friction and high wear resistance.

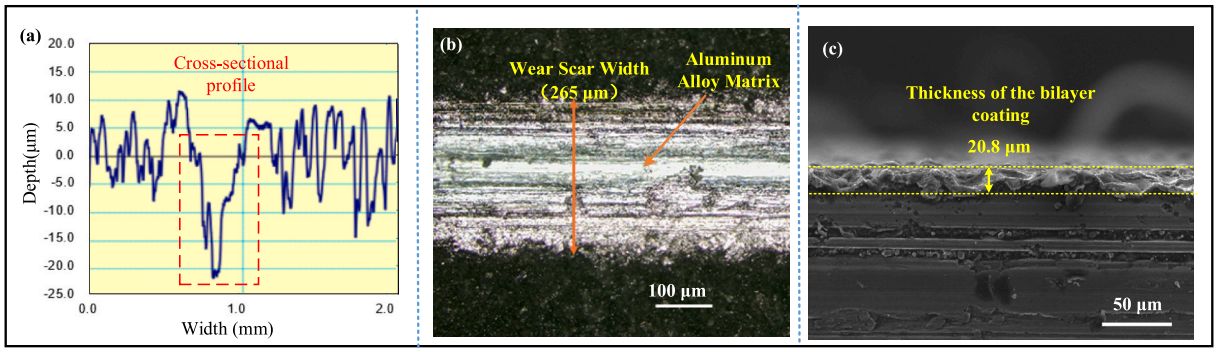

Fig. 2. Verification of the wear life criterion (COF = 0.4) for the sample prepared at 2 μs pulse duration: (a) Cross-sectional depth profile of the wear scar at failure; (b) Optical micrograph of the wear scar; (c) Cross-sectional SEM image of the original bilayer coating (20.8 μm).

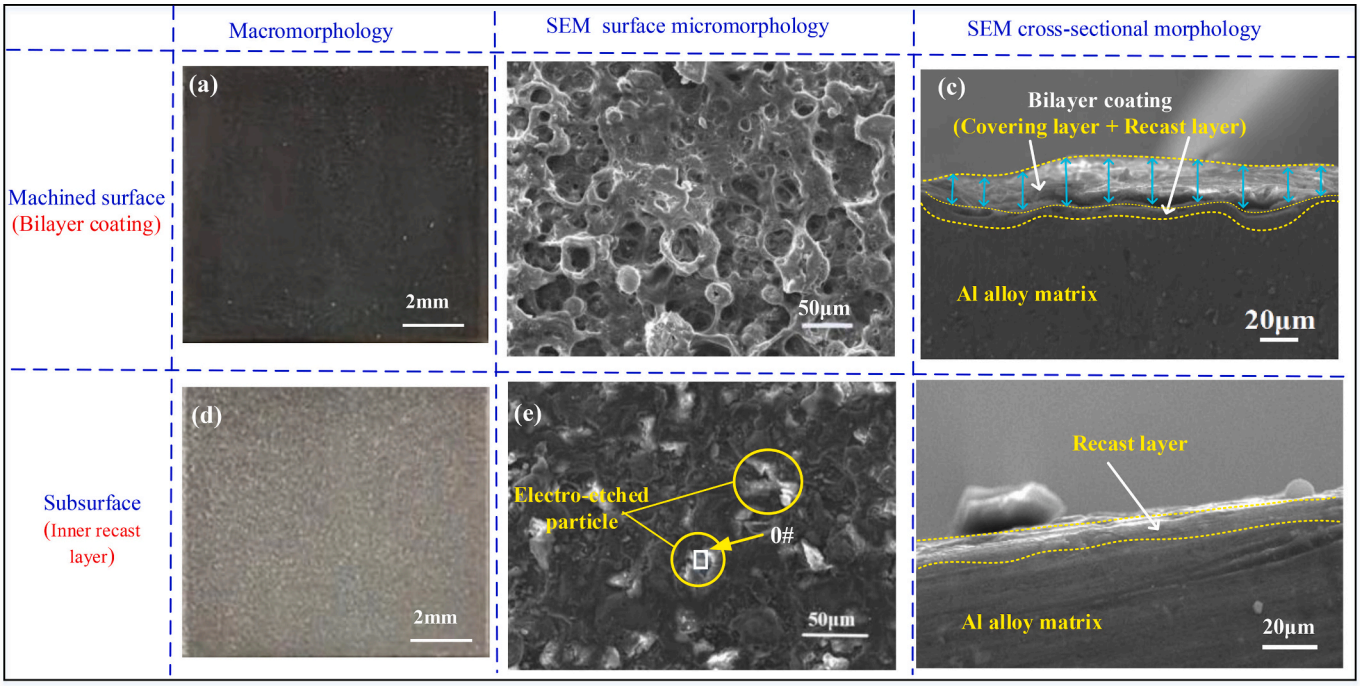

Fig. 3. Macro-morphology, surface SEM micrographs, and cross-sectional SEM images of the as-prepared coatings: (a-c) Bilayer coating with intact soft covering layer and hard recast layer; (d-f) Inner recast layer after complete removal of the soft covering layer.

Table 3
Tribological properties and one-way ANOVA results of bilayer coatings fabricated at different pulse durations.

Pulse Duration (μs)	Mean Steady-State Coefficient of Friction (COF)	Wear Life (min)
2	0.186 ± 0.0093^{a}	41 ± 2.46^{b}
4	0.185 ± 0.0092^{a}	45 ± 2.70^{c}
6	0.189 ± 0.0095^{a}	66 ± 3.96^{d}
10	0.165 ± 0.0083^{b}	34 ± 2.04^{e}
12	0.143 ± 0.0072^{c}	27 ± 1.62^{f}

Notes
(1) All data are expressed as mean ± standard deviation (SD) from three independent replicates ($n = 3$).
(2) Values with different superscript letters in the same column are significantly different (one-way ANOVA followed by LSD post-hoc test, $p < 0.05$); values with the same letter indicate no statistically significant difference.
(3) One-way ANOVA results: pulse duration has a highly significant effect on the steady-state COF ($F = 15.12$, df1 = 4, df2 = 10, $p < 0.001$) and wear life ($F = 127.90$, df1 = 4, df2 = 10, $p < 0.001$).

4.1.2. Elemental distribution and composition analysis

EDS mapping and line scan analyses were performed across the coating cross-section to verify the bilayer structure and reveal elemental distribution characteristics, as displayed in Fig. 4. For the intact bilayer coating (Fig. 4a), EDS mapping shows a pronounced elemental gradient along the depth direction. Al, as the substrate element, shows a strong signal in the Al 6061 matrix and decreases sharply toward the coating surface, clearly defining the matrix/coating interface. C is highly concentrated in the outer covering layer, mainly derived from thermal decomposition of the emulsion and intrinsic carbon in SiC nanoparticles. O is uniformly distributed across the entire coating, originating from oxidation of molten Al under transient high-temperature discharge conditions. The Si content in the covering layer is significantly higher than that in the substrate, confirming successful incorporation of SiC nanoparticles during discharge. S is weakly distributed in the outer region, corresponding to residual SDBS surfactant from the nanofluid dielectric.

Quantitative EDS line scan results (Fig. 4(c)) further validate the elemental gradient and layered structure dimensions in the maximum thickness region of Sample S3 (fabricated at a pulse duration of 6 μs,

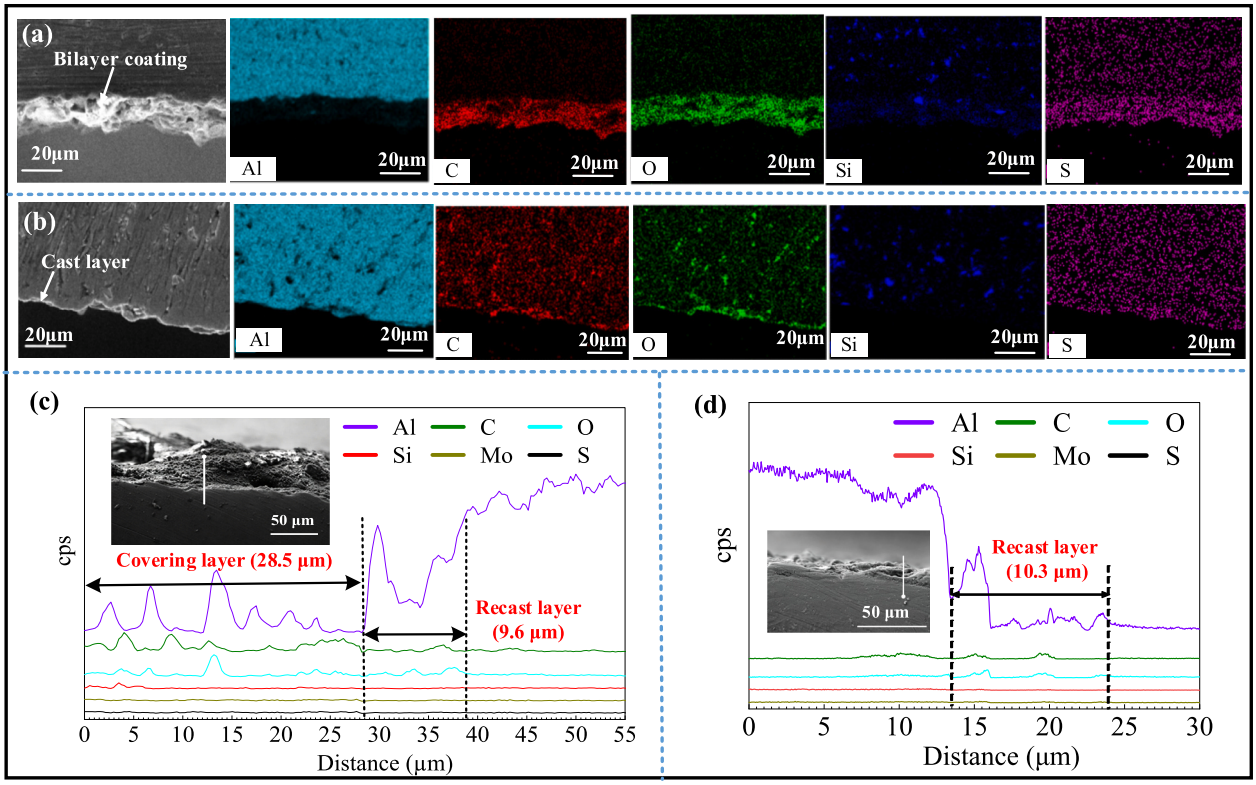

Fig. 4. EDS mapping and line scan results: (a, c) Bilayer coating (sample prepared at 6 μs pulse duration, maximum thickness region); (b, d) Inner recast layer after removing the soft covering layer via toothpaste slurry scrubbing.

consistent with the test region in Section 4.1.1): the 0–28.5 μm region corresponds to the soft covering layer with strong C and Si characteristic signals; the 28.5–38.1 μm region corresponds to the compact recast layer (9.6 μm) with a sharply rising Al signal; the region below 38 μm is the Al 6061 alloy substrate. The 6 μm deviation between the EDS (28.5 μm, maximum thickness region) and SEM (22.5 μm, full-section average) thickness results arises from differences in test regions and intrinsic characterization principles. SEM defines the coating boundary via physical morphology, while EDS uses elemental gradients, with slight carbon interdiffusion widening the C signal range.

For the inner recast layer (Fig. 4b, d), distinct signals of C and O are detected in the 12–22.3 μm region, corresponding to a recast layer thickness of approximately 10.3 μm, which matches well with that in the intact bilayer coating.

Collectively, EDS results confirm that charged species (SiC nanoparticles, oil droplets, anionic groups) in the dielectric migrate and accumulate under the electric field, participate in discharge-induced melting and metallurgical reactions, and ultimately contribute to the in-situ formation of the bilayer coating.

4.1.3. Phase composition and chemical structure analysis

Phase composition and chemical structure of the coatings were analyzed by XRD and Raman spectroscopy, as illustrated in Fig. 5. The Al 6061 substrate only shows characteristic diffraction peaks of α-Al (Fig. 5a). After removing the soft covering layer, the recast layer exhibits new diffraction peaks corresponding to Al_2O_3, verifying the formation of a ceramic-reinforced sublayer. For the intact bilayer coating, additional diffraction peaks assigned to β-SiC are detected, confirming successful incorporation of SiC nanoparticles.

To identify the phase constituents of the soft covering layer, powder scraped from the coating surface was tested by XRD (Fig. 5b). A broad diffraction hump centered at ~26° ascribed to the (002) plane of graphite-like carbon (GLC) is observed, indicating the formation of amorphous or weakly graphitized carbon phases. Weak peaks of Al_2O_3, β-SiC, and SiO_2 are also detected, suggesting that hard inclusions are embedded in the soft carbon matrix to enhance load-bearing capacity via dispersion strengthening.

Raman spectra (Fig. 5c) provide direct evidence for self-lubricating phases. The bilayer coating shows prominent D (~1350 cm^{-1}) and G (~1580 cm^{-1}) bands characteristic of sp^2-hybridized GLC, which account for the low friction behavior. Characteristic peaks of -CH- and -OH groups are also observed, indicating that the covering layer is a polar-rich organic-inorganic composite system. In contrast, the inner recast layer shows weak carbon-related signals and is dominated by inorganic ceramic phases.

These results validate the heterogeneous phase gradient: the hard Al_2O_3-rich recast layer provides mechanical support and load-bearing capability, while the carbon-rich outer layer delivers enhanced self-lubricating performance. No brittle intermetallic phases are detected, which is beneficial to the structural integrity and mechanical stability of the coating.

4.1.4. Basic mechanical properties

To elucidate the structure-property correlation of the bilayer coating and reveal the mechanical origin of its excellent tribological performance, the layer-dependent microhardness and coating-substrate interfacial bonding strength were systematically evaluated in this section.

4.1.4.1. Microhardness and layer-dependent mechanical behavior. Microhardness measurements were performed on individual layers, and the corresponding indentation morphologies are shown in Fig. 6. The maximum indentation depth is 16.21 μm (Fig. 6(b)), which is less than 3/4 of the average thickness of the soft covering layer (22.5 μm), confirming that the measured hardness reflects the intrinsic mechanical property of the covering layer without substrate interference. No chipping or cracks are observed at the indentation edge, demonstrating favorable plasticity and toughness of the soft covering layer, which

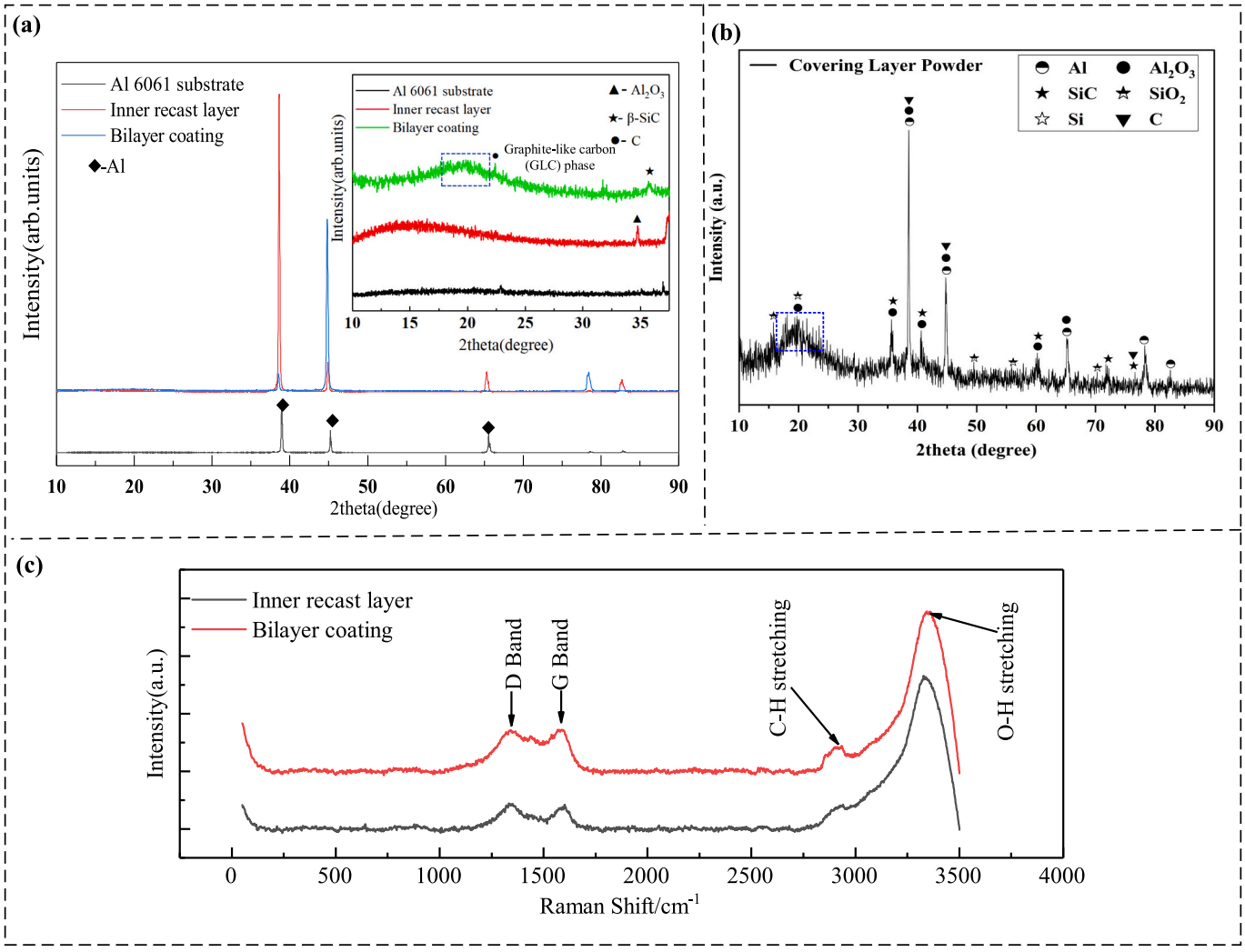

Fig. 5. Phase and chemical structure characterizations: (a) XRD patterns of the Al 6061 substrate, inner recast layer, and complete bilayer coating; (b) XRD pattern of powder scraped from the soft covering layer; (c) Raman spectra of the bilayer coating and inner recast layer.

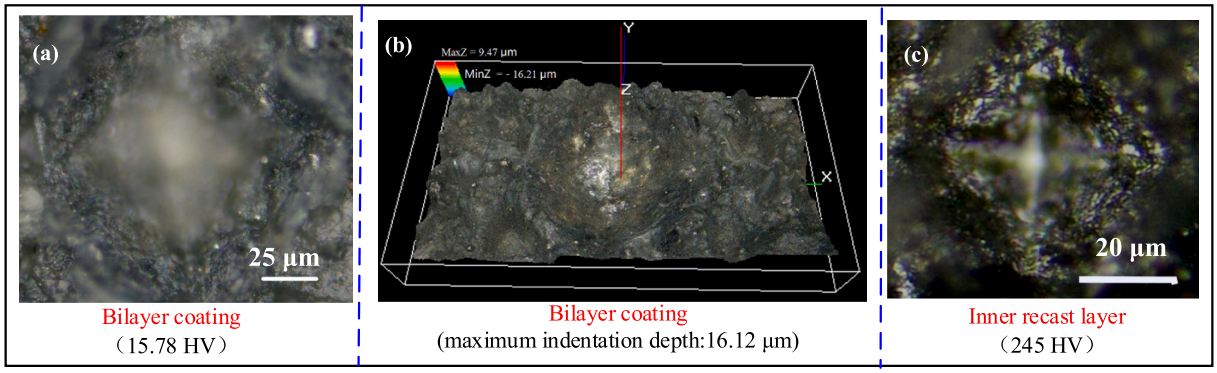

Fig. 6. Micro-indentation morphologies and corresponding microhardness values: (a) Soft covering layer of the bilayer coating; (b) 3D profile of the indentation in (a); (c) Hard inner recast layer.

favors the formation of a stable lubricating tribofilm during sliding.

In contrast, the inner recast layer exhibits a high hardness of approximately 245 HV (Fig. 6(c), with a regular Vickers indentation and no obvious cracks. The high hardness of the recast layer arises from: (i) dispersion strengthening induced by uniformly embedded Si/C-rich hard particles; (ii) a dense metallurgical structure formed during discharge remelting and rapid solidification. The high-hardness recast layer provides robust load-bearing capacity and resistance to plastic deformation.

The more than 15-fold hardness difference between the soft covering layer and hard recast layer validates the rationality of the “soft lubricating outer layer + hard load-bearing inner layer” bilayer design, which serves as the mechanical foundation for the decoupling of friction reduction and wear resistance.

4.1.4.2. Interfacial bonding strength. Interfacial bonding strength was evaluated by progressive-load scratch testing. The critical load for complete delamination (Lc2) of the bilayer coating fabricated via *E*-SiC-NFD-assisted HS-WEDM reaches 11.43 N, which is approximately 36% higher than that of the coating fabricated using pure emulsion (8.41 N). Scratch morphology observations reveal that the pure emulsion coating exhibits typical brittle interfacial failure with severe spalling at critical loads. In comparison, the E-SiC-NFD-fabricated bilayer coating only shows slight plastic deformation at Lc1 and no large-area spalling even at Lc2, presenting a progressive plastic deformation failure mode.

The enhanced interfacial bonding strength is attributed to two synergistic effects: (i) robust metallurgical bonding between the particle-reinforced recast layer and the Al alloy substrate; (ii) the stress-buffering effect of the upper soft covering layer, which suppresses catastrophic brittle fracture of the coating under high contact loads.

4.2. Evolution of soft covering layer thickness and microhardness with pulse duration

The deposition behavior and mechanical properties of the in-situ formed soft covering layer are fundamentally dominated by pulse duration-related effects. Specifically, variations in pulse duration simultaneously adjust two core components of the effects: the single-pulse discharge energy, and the effective time window for electrophoretic migration of charged species in the E-SiC-NFD dielectric. These two factors co-determine the thickness and microhardness of the soft covering layer, and their evolution with varying pulse duration is systematically investigated in this section. All data are presented as mean ± standard deviation from triplicate independent measurements.

As shown in Fig. 8(a), the thickness of the soft covering layer increases monotonically from 16.5 μm (2 μs) to 22.16 μm (12 μs) with extended pulse duration, with a gradually decelerated growth rate. This trend arises from two coupled effects: (i) longer pulse duration widens the time window for charged species to migrate and accumulate on the workpiece surface, supplying more precursors for coating deposition; (ii) elevated discharge energy intensifies substrate melting and vaporization, generating more molten products for surface redeposition. The slowed growth rate above 6 μs is attributed to saturated electrophoretic accumulation, and enhanced ejection of deposited materials by high-energy discharge. Notably, the average thickness of the 6 μs optimal sample measured by the eddy current method (20.25 μm) is slightly lower than the cross-sectional SEM-measured average thickness (22.5 μm), which arises from the intrinsic difference between bulk eddy current thickness testing and local cross-sectional SEM measurement.

The microhardness of the soft covering layer exhibits a distinct non-monotonic trend with increasing pulse duration, peaking at 15.78 HV at the moderate pulse duration of 6 μs. This evolution is essentially regulated by the particle embedding behavior, which is controlled by pulse duration-related effects. At 6 μs, the discharge energy and migration time matched by the effects maximize the uniform embedding and stable retention of hard electro-eroded particles, delivering the strongest dispersion strengthening effect. In contrast, excessive pulse durations (10–12 μs) induce severe melt pool turbulence and intense discharge explosive force, causing massive ejection of embedded particles, weakening the strengthening effect and reducing the microhardness of the soft covering layer.

4.3. Oil-free tribological performance and wear mechanism of the bilayer coatings

Dry sliding tribological tests were carried out under a 5 N normal load against a 6 mm-diameter Si_3N_4 ball, as described in Section 3.4.5. This section systematically investigates the effects of pulse duration on the coefficient of friction (COF), wear life, and wear mechanism of the in-situ fabricated bilayer coatings. Combined with microstructural and mechanical characteristics in Sections 4.1 and 4.2, the structure–performance relationship and the decoupling mechanism between friction reduction and wear resistance are clarified. All tests were performed in triplicate, and data are presented as mean ± standard deviation.

4.3.1. Friction coefficient and wear life

Fig. 9(a) presents the time-dependent coefficient of friction (COF) curves of the bilayer coatings fabricated at different pulse durations. All samples exhibit three typical friction stages: a short running-in period, a long steady-state friction stage, and a sharp rise in COF corresponding to coating failure. Consistent with the definition in Section 3.4.5, the wear life in this work is defined as the total sliding duration when the COF first exceeds the critical failure threshold of 0.4.

Compared with the Al 6061 substrate (COF = 0.621 [31]), all as-fabricated bilayer coatings achieved a 68.9%–77.0% reduction in steady-state COF (Fig. 9(b)). The steady-state COF showed a two-stage evolution trend with increasing pulse duration. For pulse durations ranging from 2 μs to 6 μs, the steady-state COF remained stable in the range of 0.185–0.189, with no statistically significant difference between groups (one-way ANOVA, $p > 0.05$, consistent with the identical superscript letters in Table 4). In contrast, when the pulse duration exceeded 6 μs, the steady-state COF decreased significantly ($p < 0.05$), reaching a minimum value of 0.143 at a pulse duration of 12 μs.

The wear life of the coatings showed a distinct non-monotonic trend with increasing pulse duration (Fig. 9(c)), peaking at 66 min for the 6 μs sample, and decreasing continuously to 27 min at 12 μs. This evolution trend is highly consistent with the microhardness change of the soft covering layer (Section 4.2), confirming that the dispersion strengthening effect and load-bearing capacity of the coating are the dominant factors governing wear life.

Detailed tribological properties and statistical analysis results of the coatings are summarized in Table 3. One-way analysis of variance (ANOVA) confirms that pulse duration has a highly significant effect on both steady-state COF ($F = 15.12$, $p < 0.001$) and wear life ($F = 127.90$, $p < 0.001$). Post hoc least significant difference (LSD) multiple comparisons further verify that the coating fabricated at 6 μs exhibits a significantly longer wear life than all other groups ($p < 0.05$), while the 12 μs sample yields a significantly lower steady-state COF than all other groups ($p < 0.05$).

A critical original finding of this work is that the minimum steady-state COF and maximum wear life do not occur at the same process parameter, as they are governed by two independent competing mechanisms, both of which are regulated by pulse duration-related effects. Specifically, the COF is dominated by the formation of graphite-like self-lubricating carbon phases, which is enhanced by the elevated single-pulse discharge energy from extended pulse duration; while the wear life is fundamentally determined by the mechanical strength of the coating and interlayer interfacial integrity, which is maximized under the moderate pulse duration-related effects at 6 μs. An excessively long pulse duration (12 μs) promotes the formation of lubricating phases, but degrades the embedding efficiency of hard particles and the structural stability of the coating, leading to premature failure. This decoupling mechanism provides a flexible design principle for tailoring the coating performance to match specific service requirements.

4.3.2. Wear mechanism under oil-free dry sliding

Worn surface morphologies (Fig. 10) reveal that the wear mechanism is controlled by the embedding state of electro-eroded particles, which is essentially dominated by pulse duration-related effects. ImageJ quantification shows particle area fractions of 13.2%, 17.12%, and 13.15% at 2, 6, and 12 μs, respectively, consistent with hardness and wear life trends.

The 2 μs sample (S1) exhibits slight ploughing and minimal debris, corresponding to mild abrasive wear due to insufficient dispersion strengthening. The 6 μs sample (S3) shows uniform, shallow plastic ploughing without spalling or cracking. The high content of well-bonded

Table 4
EDS point scan results of electro-eroded particles on coatings prepared at different pulse durations (wt%).

Sample No.	Pulse duration (μs)	Chemical composition(wt%)							
		C	O	Al	Si	S	Mo	K	Mg
S3 (Fig. 3e, 0#)	6	35.68	28.13	30.72	1.64	0.01	1.87	0.74	0.31
S1(1#)	2	51.45	34.09	11.99	1.16	0.78	0.11	0.29	0.13
S3(2#)	6	33.66	33.42	28.70	2.19	1.19	0.32	0.30	0.22
S5(3#)	12	42.17	32.31	20.54	2.33	1.33	0.42	0.74	0.16

hard particles effectively supports the load and suppresses severe wear, consistent with the longest wear life. The 12 μs sample (S5) displays severe plastic deformation, massive debris accumulation, and interfacial cracks around coarse particles. These poorly bonded particles are easily extruded, causing severe three-body abrasive wear and fatigue spalling, which drastically shortens wear life despite the low COF. EDS analysis (Table 4) shows that Si content increases from 1.16 wt% (2 μs) to 2.33 wt % (12 μs), confirming that pulse duration governs the migration and incorporation of SiC nanoparticles, thereby dominating the coating's tribological behavior.

In summary, pulse duration tailors the tribological performance by regulating particle embedding and lubricating phase formation. A moderate pulse duration of 6 μs achieves the optimal balance between strengthening and lubrication, leading to the best comprehensive wear resistance.

4.4. Formation mechanism and property evolution framework of the bilayer coating

Based on the systematic characterization of microstructure, mechanical properties, and tribological performance in Sections 4.1–4.3, this section establishes the in-situ formation mechanism of the bilayer coating during *E*-SiC-NFD-assisted HS-WEDM, elucidates the Pinning-Locking interfacial strengthening mechanism, and proposes a unified mechanistic framework to clarify the regulatory effect of pulse duration on the coating's structure and tribological performance.

4.4.1. In-situ autogenesis process of the bilayer coating

The heterogeneous bilayer structure is formed in situ during the pulsed discharge cycles of HS-WEDM, without any additional post-treatment. As shown in Fig. 11, the formation process is divided into four sequential stages, each of which is supported by our experimental characterization results:

(1) **Electrophoretic migration and accumulation stage** (Fig. 11 (a)): Under the applied pulse voltage, negatively charged SiC nanoparticles, oil droplets, and anionic groups in the *E*-SiC-NFD dielectric migrate toward the positive workpiece anode, and accumulate on the machined surface. This process is verified by the zeta potential test result (−36 mV) of the nanofluid, which confirms the excellent surface charge characteristics and migration capacity of the charged species.

(2) **Dielectric breakdown and discharge channel formation stage** (Fig. 11(b)): The accumulated charged species form a conductive adsorption layer on the workpiece surface, which shortens the effective inter-electrode gap and distorts the local electric field, significantly reducing the breakdown voltage and facilitating dielectric breakdown. A high-temperature discharge channel (8000–15,000 °C) is instantaneously formed, which melts the Al alloy substrate surface to generate a micro-molten pool, and provides sufficient thermodynamic conditions for the in-situ oxidation and pyrolysis reactions of dielectric components in the subsequent stage.

(3) **In-situ reaction and deposition stage** (Fig. 11(c)): The instantaneous high temperature of the discharge triggers synchronous melting, oxidation, and pyrolysis reactions in the discharge gap and molten pool. The oxidation reaction of SiC nanoparticles during discharge is as follows:

$$SiC + 2O_2 \rightarrow SiO_2 + CO_2 \quad (1)$$

This reaction generates SiO_2, a hard ceramic phase that enhances the hardness and wear resistance of the recast layer, and CO_2. Meanwhile, part of SiC undergoes incomplete thermal decomposition under oxygen-deficient conditions in the micro-molten pool, generating free graphite-like sp^2-hybridized carbon, which is the core self-lubricating phase of the coating and supplements the carbon source for the formation of the carbonaceous lubricating film. In addition, the Al substrate melts and oxidizes to form Al_2O_3 ceramic phase, and the mineral oil in the emulsion pyrolyzes to form abundant graphite-like carbon phases. During this process, the molten reaction products and unreacted SiC nanoparticles redeposit on the machined surface to form the soft covering layer, while the residual molten pool on the substrate surface rapidly solidifies to form the dense recast layer.

(4) **Cooling and solidification stage** (Fig. 11(d))**:** During the pulse interval, the high-thermal-conductivity nanofluid achieves rapid cooling of the machined surface, completing the non-equilibrium solidification of the bilayer coating, and resetting the inter-electrode conditions for the next discharge cycle.

4.4.2. Bilayer coating structure model and pinning-locking interfacial strengthening mechanism

Based on the multi-scale structural and mechanical characterization results in the preceding sections, a heterogeneous bilayer structure model is constructed (as shown in Fig. 12), and the core Pinning-Locking interfacial strengthening mechanism is systematically elucidated.

4.4.2.1. Bilayer coating structure model. The cross-sectional SEM image in Fig. 12(a) directly validates the intact bilayer architecture: the as-fabricated bilayer coating consists of two functional layers with completely differentiated composition and properties: an upper soft self-lubricating covering layer and a lower hard load-bearing recast layer, where the recast layer forms a robust metallurgical bonding with the Al 6061 alloy matrix:

Hard load-bearing recast layer. The bottom layer adjacent to the Al 6061 matrix is a dense recast layer, which forms defect-free metallurgical bonding with the alloy matrix. XRD results (Section 4.1.3, Fig. 5 (a)) confirm that the recast layer is dominated by hard Al_2O_3 ceramic reinforcement phase, with numerous containing electro-eroded particles uniformly embedded inside (Fig. 12(c)). The surface of the recast layer features abundant micron-scale discharge craters and microcracks (marked in Fig. 12(a)), which are inherent defects induced by the extremely rapid heating-cooling thermal cycles at discharge spots during the HS-WEDM process. These surface micro-defects not only provide physical sites for the deposition and filling of the upper covering layer, but also the embedded SiC hard phase gives the recast layer a high microhardness of ~245 HV (Section 4.1.4, Fig. 6(c)), which provides stable load-bearing capacity for the entire coating system during friction.

Soft self-lubricating covering layer. The top layer is a soft covering layer, which is tightly adhered to the surface of the recast layer. XRD and Raman spectroscopy results (Section 4.1.3, Fig. 5(b, c)) confirm that the covering layer is a carbon-based composite matrix dominated by sp^2-hybridized graphite-like carbon (GLC) self-lubricating phase, with β-SiC, Al_2O_3 and SiO_2 hard particles uniformly dispersed inside. This phase

composition gives the covering layer an ultra-low microhardness of ~15.78 HV (Section 4.1.4, Fig. 6(a)), which is only 1/15 of the recast layer hardness, showing excellent softness and ductility. As shown in Fig. 12(b), the excellent plastic deformability of the GLC matrix enables it to fully penetrate and fill the micron-scale discharge craters, microcracks and micropores on the recast layer surface, which lays a direct structural foundation for the formation of the Pinning-Locking effect.

4.4.2.2. Core synergistic pinning-locking interfacial strengthening mechanism. The superior interfacial bonding performance and structural stability between the soft covering layer and the hard recast layer are dominated by the following two synergistic sub-effects, which are fully supported by the indentation and scratch test results in Section 4.1.4, and collectively enhance the service reliability of the bilayer coating under oil-free friction:

Pinning Strengthening Effect: The soft GLC-based material of the covering layer fully fills and embeds into the microcracks and micropores on the recast layer surface (marked in Fig. 12(a)). During friction and external loading, the embedded soft material acts as "pinning nails", which effectively inhibits the initiation and propagation of cracks within the hard brittle recast layer, reduces the brittle cracking tendency of the coating, and significantly improves the structural integrity and damage resistance of the recast layer. This effect is directly verified by the mechanical test results in Section 4.1.4: the indentation on the recast layer shows a standard Vickers morphology without radial cracks (Fig. 6(c)), confirming the suppressed brittle cracking tendency; meanwhile, the complete and smooth wear track morphology in the OM image of Fig. 12 (a) shows no large-area brittle spalling of the coating after long-term friction, which further validates the pinning strengthening effect.

Locking Anchoring Effect: This effect is realized by the synergistic action of mechanical interlocking and chemical bonding, which significantly improves the interlayer interfacial bonding strength: (i) **Mechanical interlocking anchoring**: The micron-scale discharge craters on the recast layer surface provide abundant 3D interlocking sites for the deposition of the soft covering layer, forming a stable physical anchoring structure between the two layers, which prevents the relative sliding of the covering layer under shear force during friction. (ii) **Chemical bonding enhancement**: Raman spectroscopy in Section 4.1.3 and FTIR analysis from our previous study [31] confirms that the soft covering layer contains abundant strong polar hydroxyl groups, which can form stable chemical bonding with the metal oxide phases (Al_2O_3) in the recast layer (verified by XRD in Section 4.1.3), further strengthening the interlayer bonding at the atomic scale.

This effect is quantitatively validated by the progressive-load scratch test results in Section 4.1.4 (Fig. 7): the critical delamination load (Lc2) of the bilayer coating reaches 11.43 N, which is approximately 36% higher than that of the single-layer coating fabricated with pure emulsion. Meanwhile, the coating presents a progressive plastic deformation failure mode without large-area brittle spalling even at the critical load, which directly confirms the significant enhancement of interfacial bonding strength via the Locking Anchoring effect.

The synergistic Pinning-Locking effect fundamentally solves the key contradiction between the low friction of the soft lubricating layer and the high load-bearing of the hard recast layer, and realizes the stable service of the bilayer coating under long-term oil-free dry sliding conditions.

4.4.3. Property evolution mechanism regulated by pulse duration-related effects

We propose a unified mechanistic framework to clarify the non-monotonic, non-synchronized evolution of the coating's mechanical and tribological properties (Fig. 13). In this framework, pulse duration-related effects, rather than the single pulse duration parameter, act as the core regulatory switch for coating structure and performance. Variations in pulse duration simultaneously trigger coupled physical and chemical changes in the discharge gap, which collectively form the pulse duration-related effects. These effects include four core components: (1) Variation in single-pulse discharge energy, which determines molten pool temperature, lifetime, and the pyrolysis/oxidation degree of dielectric components; (2) Variation in effective electrophoretic migration time, which dominates the accumulation of charged SiC nanoparticles and oil droplets on the workpiece surface; (3) Variation in workpiece heat accumulation and material removal behavior, which affects recast layer solidification and covering layer redeposition; (4) Variation in dielectric flow field state and local particle concentration in the discharge gap, which affects the uniformity of particle embedding and coating formation.

These coupled effects simultaneously govern two competing processes in the discharge zone: dispersion strengthening from particle embedding, and friction reduction from self-lubricating phase formation. The non-synchronized evolution of COF and wear life essentially arises from the differing sensitivity of these two processes to pulse duration-related effects.

At a moderate pulse duration of 6 μs, the effects achieve an optimal balance between discharge energy and migration time. This balance promotes uniform embedding and stable retention of hard electro-eroded particles in the soft covering layer, reaching a maximum particle area fraction of 17.12%. The dispersion strengthening effect is thus maximized, endowing the covering layer with a peak microhardness of 15.78 HV and optimal load-bearing capacity. Meanwhile, the stable discharge conditions under this moderate pulse duration support the formation of an intact covering layer and robust interlayer bonding, resulting in the maximum wear life of 66 min.

At an excessive pulse duration of 12 μs, amplified pulse duration-related effects increase single-pulse discharge energy. The extended molten pool lifetime promotes emulsion pyrolysis, generating more graphite-like self-lubricating carbon phases. This reduces interfacial

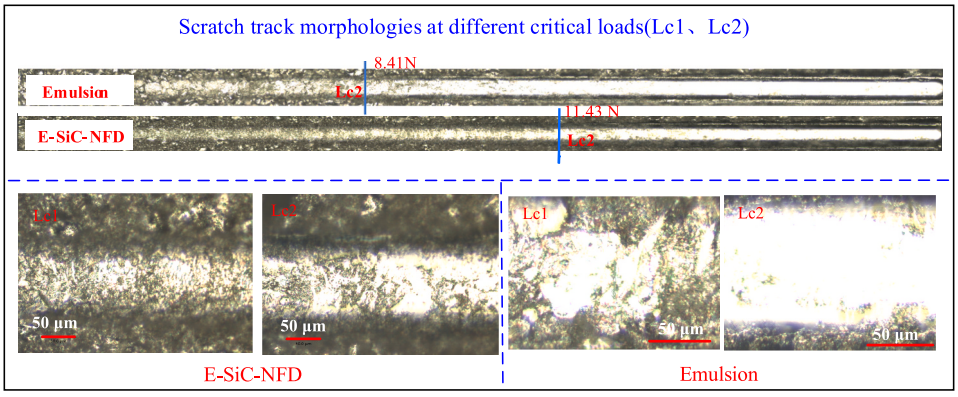

Fig. 7. Scratch track morphologies of coatings prepared using pure emulsion and *E*-SiC-NFD dielectric under critical loads Lc1 and Lc2.

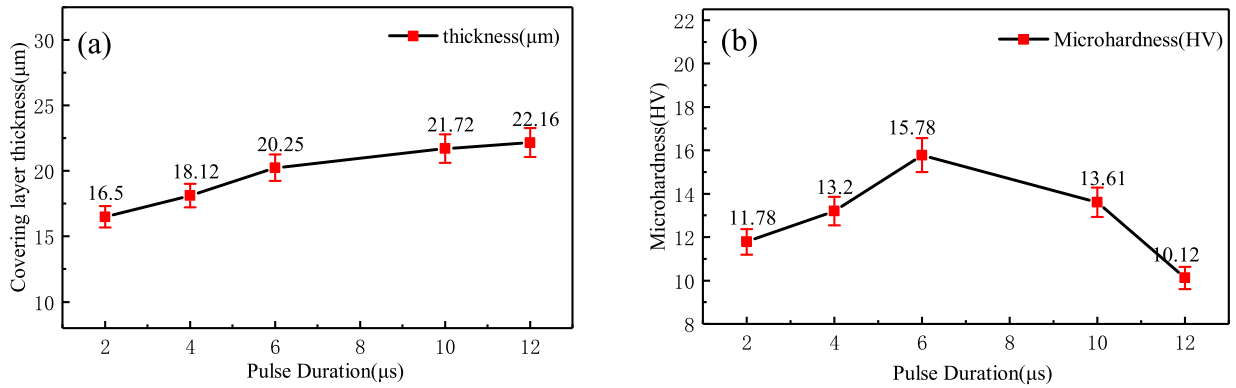

Fig. 8. Evolution of (a) thickness and (b) microhardness of the soft covering layer as functions of pulse duration.

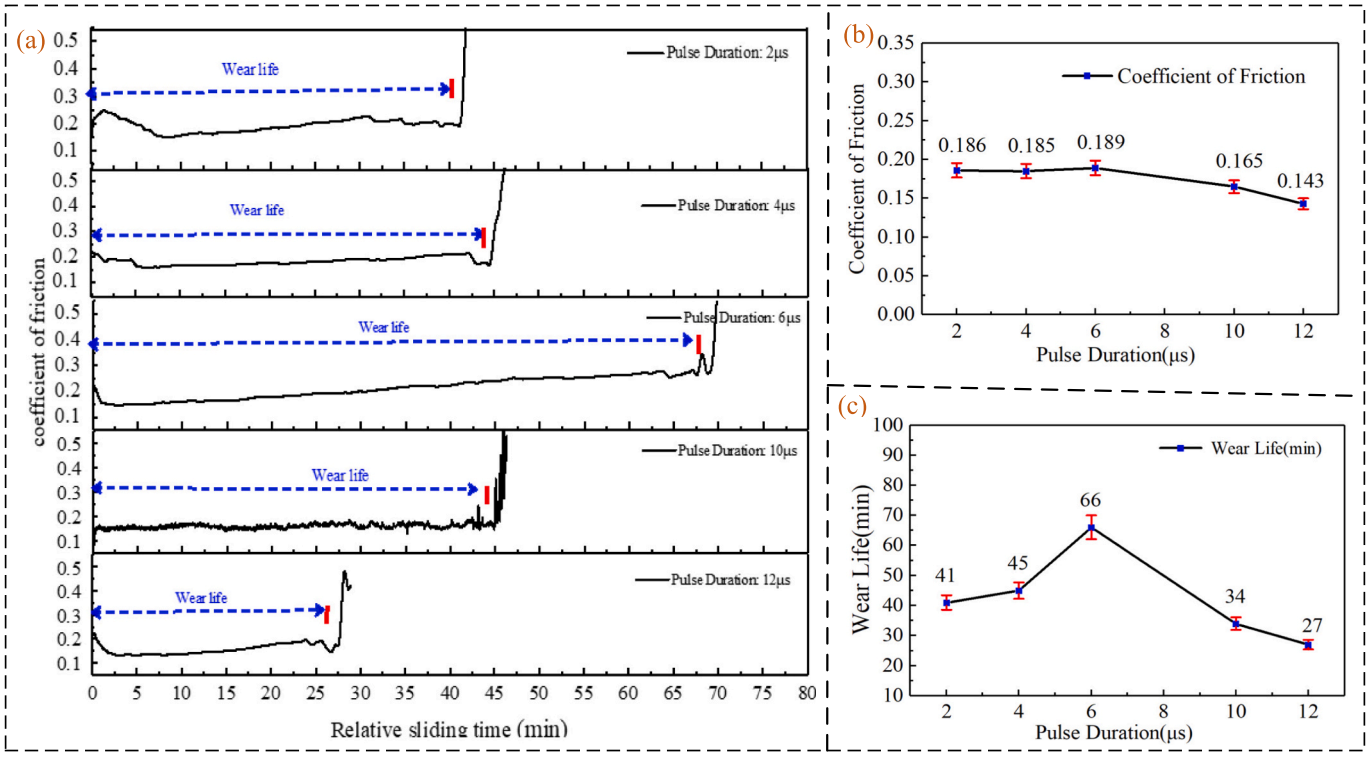

Fig. 9. Tribological performance of the bilayer coatings: (a) Time-dependent COF curves; (b) Steady-state COF values; (c) Wear life values at different pulse durations.

shear stress during sliding, achieving the minimum COF of 0.143. However, the amplified effects also induce severe molten pool turbulence and intense discharge explosive force, causing massive ejection of embedded hard particles (particle area fraction reduced to 13.15%). This weakens the dispersion strengthening effect and degrades the coating's mechanical strength. Meanwhile, the severe thermomechanical cycling introduces interfacial micro-defects, leading to premature coating failure and a significantly shortened wear life of 27 min.

This framework coherently explains the core finding of this work: the lowest COF and longest wear life do not coincide, as they are governed by two competing mechanisms regulated by pulse duration-related effects. COF is dominated by the formation of self-lubricating carbon phases, while wear life is fundamentally determined by particle-induced dispersion strengthening and interlayer interfacial integrity.

It should be noted that this decoupling mechanism has the most significant performance in the in-situ autogenous coating system prepared by EDM, because the formation of lubricating phases and the dispersion strengthening of the coating are simultaneously regulated by the pulse duration-related effects of discharge parameters, showing a clear competitive relationship under different energy inputs. This mechanism framework can also be extended to other composite coating systems where the lubricating phase content and matrix mechanical strength are regulated by the same process parameter.

5. Conclusions

A bilayer wear-resistant coating was in-situ fabricated on an Al 6061 alloy substrate via HS-WEDM with the *E*-SiC-NFD, which resolves the critical bottleneck of conventional aluminum alloy surface modification technologies that cannot synergistically achieve low friction and high wear resistance. The core conclusions of this study are summarized as follows:

(1) A heterogeneous bilayer structure, consisting of a soft carbon-rich self-lubricating covering layer and a hard Al_2O_3-rich load-bearing recast

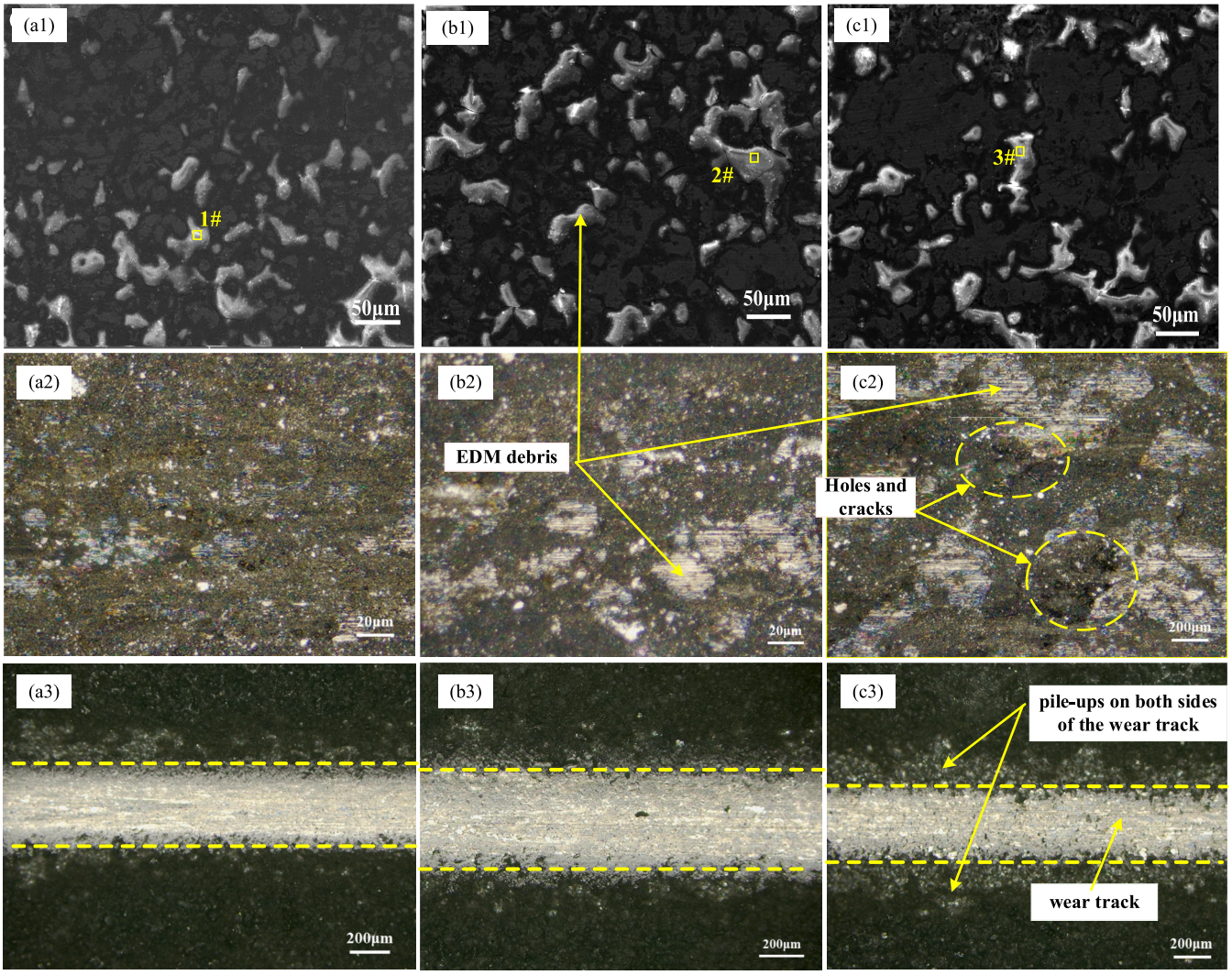

Fig. 10. Multi-scale morphologies of worn surfaces: (a1-c1) SEM images; (a2-c2) Optical micrographs at 500× magnification; (a3-c3) Optical micrographs at 100× magnification for samples S1, S3, and S5.

layer, is spontaneously formed in-situ during the HS-WEDM pulsed discharge cycle without any secondary post-treatment. The soft covering layer fully fills the micro-defects on the recast layer surface, and the interlayer interfacial bonding strength is significantly enhanced via the synergistic Pinning-Locking effect, which endows the coating with excellent structural stability and damage resistance.

(2) Pulse duration-related effects serve as the core governing factor for the deposition behavior, microstructure and mechanical properties of the bilayer coating. The thickness of the soft covering layer increases monotonically with extended pulse duration, while its microhardness exhibits a distinct non-monotonic trend, peaking at 15.78 HV at a moderate pulse duration of 6 μs. The regulatory law of pulse duration-related effects on the coating's structure and properties provides a clear process window for the industrial application of this technology.

(3) A key original finding of this work is that the minimum steady-state COF and maximum wear life do not coincide, as they are governed by two independent competing mechanisms. The COF is primarily determined by the formation of graphite-like self-lubricating carbon phases, which is optimized at a pulse duration of 12 μs (minimum COF of 0.143); in contrast, the wear life is fundamentally dominated by the particle-induced dispersion strengthening and interlayer interfacial integrity, which are maximized at 6 μs (longest wear life of 66 min). This decoupling mechanism provides a flexible design principle for tailoring the coating performance to match specific oil-free service requirements.

(4) The E-SiC-NFD-assisted HS-WEDM technology developed in this work achieves one-step integration of precision forming and in-situ surface strengthening of aluminum alloys. The as-fabricated bilayer coating delivers a steady-state COF as low as 0.143 and a wear life up to 66 min under oil-free dry sliding conditions, providing a novel, low-cost and high-efficiency technical pathway for the wear-resistant modification of lightweight aluminum alloys used in aerospace, automotive and other harsh oil-free working conditions.

CRediT authorship contribution statement

Cuixia Guo: Methodology, Data curation, Writing – original draft. **Gui He:** Investigation, Formal analysis, Software. **Jianping Zhang:** Project administration, Data curation, Investigation. **Xinjun Zhou:** Formal analysis, Validation, Writing – review & editing. **Shixue Zhang:** Data curation, Formal analysis. **Zhangyong Wu:** Methodology, Funding acquisition, Resources.

Consent to participate

Not applicable.

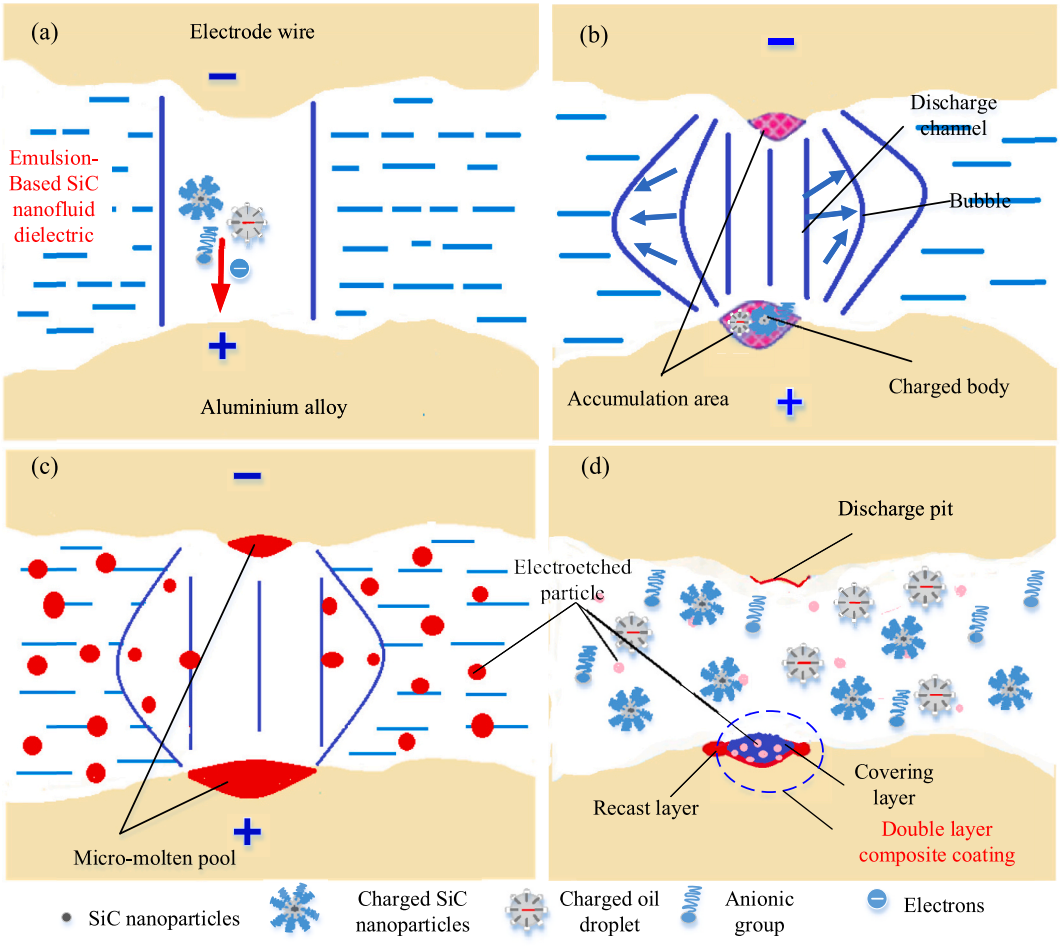

Fig. 11. Schematic of single-pulse discharge and in-situ coating formation during E-SiC-NFD-assisted HS-WEDM: (a) Migration and accumulation of charged species; (b) Dielectric breakdown and micro molten pool formation; (c) In-situ reaction and deposition of the covering layer; (d) Cooling and solidification of the bilayer coating.

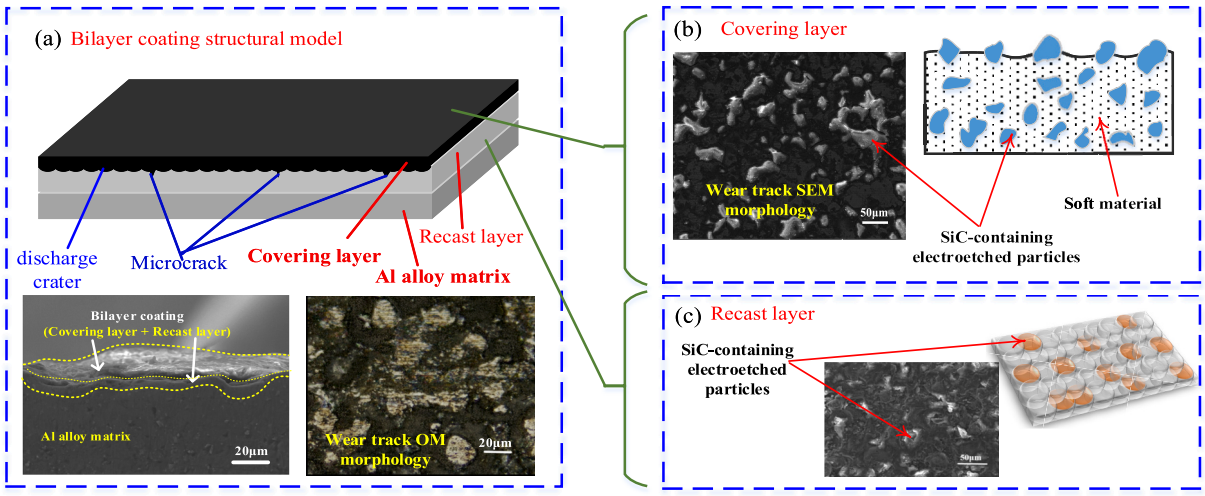

Fig. 12. Structural model of the bilayer coating: (a) Overall bilayer architecture; (b) Soft covering layer with electro-eroded particles; (c) Hard recast layer with discharge craters.

Consent to publish

Not applicable.

Ethical approval

Not applicable.

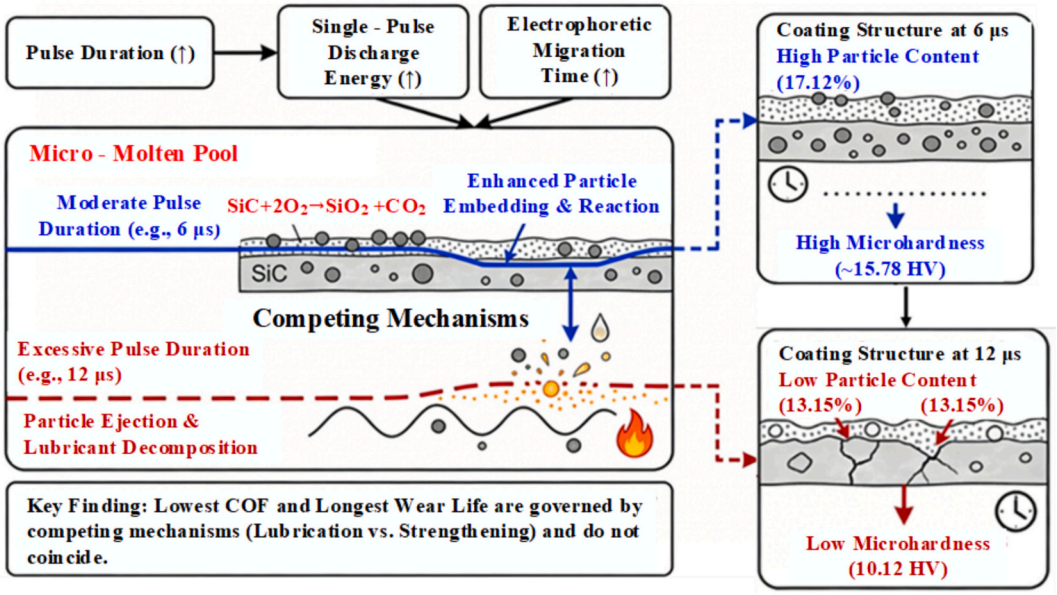

Fig. 13. Mechanistic framework illustrating the correlation between pulse duration and the tribological properties of the in-situ formed bilayer coating.

Funding

This study was supported by Sichuan Science and Technology Program (Grant No. 2026NSFSC0326), the Scientific Research and Innovation Team Program of Sichuan University of Science and Engineering (Grant No. H92322), the National Natural Science Foundation of China (Grant No. 51301115), Sichuan Provincial Key Lab of Process Equipment and Control (Grant No. GK202307), University Student Innovation and Entrepreneurship Training Program Project of Sichuan University of Science and Engineering (Grant No. cx2025069).

Declaration of competing interest

The authors declare that they have no known competing financial interests or personal relationships that could have appeared to influence the work reported in this paper.

Data availability

Data will be made available on request.

References

[1] K.U. Bhat, D.B. Panemangalore, S.B. Kuruveri, M. John, P.L. Menezes, Surface modification of 6xxx series aluminum alloys, Coatings 12 (2) (2022) 180.
[2] R. Buckingham, T. Asset, P. Atanassov, Aluminum-air batteries: a review of alloys, electrolytes and design, J. Power Sources 498 (2021) 229762.
[3] C.X. Wang, H.Q. Ni, V.C. Ji, J.L. Lei, W. Deng, P. Song, et al., Wear properties of micro-arc oxidation coatings on aluminum alloys, J. Mater. Sci. 61 (8) (2026) 4973–5007.
[4] J. Bang, E. Lee, Enhancing wear resistance of A390 aluminum alloy: a comprehensive evaluation of thermal sprayed WC, CrC, and Al_2O_3 coatings, Coatings 14 (7) (2024) 853.
[5] C.J. Liang, C.L. Wang, K.X. Zhang, M.L. Liang, Y.G. Xie, W.J. Liu, et al., Nucleation and strengthening mechanism of laser cladding aluminum alloy by Ni-Cr-B-Si alloy powder based on rare earth control, J. Mater. Process. Technol. 294 (2021) 117145.
[6] S.M. Dezfuli, M. Sabzi, Deposition of ceramic nanocomposite coatings by electroplating process: a review of layer deposition mechanisms and effective parameters on the formation of the coating, Ceram. Int. 45 (17) (2019) 21835–21842.
[7] R.K. Barooah, J.M. Paiva, A.F.M. Arif, S. Rawal, B. Bose, S.C. Veldhuis, Investigation on wear mechanisms of PVD coatings for form taps in threading of Al–Si alloy, Wear 464–465 (2021) 203528.
[8] W. Yao, L. Wu, J. Wang, B. Jiang, D. Zhang, M. Serdechnova, et al., Micro-arc oxidation of magnesium alloys: a review, J. Mater. Sci. Technol. 118 (2022) 23–56.
[9] C. Deng, Z. Liu, M. Zhang, H. Pan, M. Qiu, Study on surface evenness of super-high-thickness cutting in high-speed wire electrical discharge machining, Int. J. Adv. Manuf. Technol. 117 (11–12) (2021) 3705–3715.
[10] M. Zhang, M. Qiu, Z. Liu, Effect of interpulse voltage on recast layer machined by HSWEDM, Mater. Manuf. Process. 39 (1) (2024) 90–97.
[11] G. Su, C. Zhang, J. Li, G. Liu, X. Chen, Y. Zhang, Enhancing cutting rates in multi-channel HSWEDM of metal materials with a novel decoupling circuit, Micromachines 14 (12) (2023) 2226.
[12] R. Chaudhari, J.J. Vora, V. Patel, L.N.L. de Lacalle, D.M. Parikh, Effect of WEDM process parameters on surface morphology of nitinol shape memory alloy, Materials 13 (21) (2020) 4943.
[13] M.N. Alam, A.N. Siddiquee, Z.A. Khan, N.Z. Khan, A comprehensive review on wire EDM performance evaluation, Proc. Inst. Mech. Eng. Part E J. Process Mech. Eng. 236 (4) (2022) 1724–1746.
[14] R. Jayachitra, R. Ranjith, B. Ramesh, R. Lawanya, Surface modification of Hastelloy processed by the cu mixed electric discharge alloying technique, Surf. Eng. 38 (5) (2022) 514–523.
[15] M. Sana, M. Asad, M.U. Farooq, S. Anwar, M. Talha, Sustainable electric discharge machining using alumina-mixed deionized water as dielectric: process modelling by artificial neural networks underpinning net-zero from industry, J. Clean. Prod. 441 (2024) 140926.
[16] Z.Z. Wu, X.Y. Wu, R. Chen, Y. Yang, M. Wang, L.Y. Xu, et al., Working end wear of 3D-laminated microelectrode in reverse-polarity PMEDM with gr and cu powders, Int. J. Adv. Manuf. Technol. 131 (7–8) (2024) 3555–3564.
[17] J.T. Philip, J. Mathew, B. Kuriachen, Transition from EDM to PMEDM – impact of suspended particulates in the dielectric on Ti6Al4V and other distinct material surfaces: a review, J. Manuf. Process. 64 (2021) 1105–1142.
[18] H. Buessemaker, A.K. Meinshausen, V.D. Bui, J. Do, V. Voropai, A. Buchholz, et al., Silver-integrated EDM processing of TiAl6V4 implant material has antibacterial capacity while optimizing osseointegration, Bioact. Mater. 31 (2023) 497–508.
[19] I.A. Gul, A.M.A. Rani, F.B.A. Munir, A. Khan, M. Al-Amin, Surface characteristics and machining rate of SS 316L coating developed using hydroxyapatite-mixed EDM process, Ceram. Int. 50 (22) (2024) 35919–35929.
[20] Z. Liu, L. Li, X. Liu, J. Meng, M. Zang, Wear and corrosion resistance behavior of hydrophobic surface on Ti-6Al-4V prepared by nitrogen gas-assisted EDM, Surf. Coat. Technol. 489 (2024) 131150.
[21] G. Elhuseini, F.B. Abd Munir, A.M.A. Rani, A.A. Aliyu, H. Saputro, N.S.A.B. Roslan, et al., Zinc-manganese dual electrodischarge deposition on 316 L stainless steel: a study on surface integrity, hydrophobicity, hardness, and corrosion behaviors, Surf. Coat. Technol. 514 (2025) 132569.
[22] G. Keskin, S. Salunkhe, G. Küçüktürk, M. Pul, H. Gürün, V. Baydaroğlu, Optimization of PMEDM process parameters for B4C and B4C+SiC reinforced AA7075 composites, J. Eng. Res. 13 (1) (2025) 47–56.
[23] M.P. Mughal, M.U. Farooq, J. Mumtaz, M. Mia, M. Shareef, M. Javed, et al., Surface modification for osseointegration of Ti6Al4V ELI using powder mixed sinking EDM, J. Mech. Behav. Biomed. Mater. 113 (2021) 104145.
[24] C. Prakash, H.K. Kansal, B.S. Pabla, S. Puri, Potential of powder mixed electric discharge machining to enhance the wear and tribological performance of β-Ti implant for orthopedic applications, J. Nanoeng. Nanomanuf. 5 (4) (2015) 261–269.
[25] C.A.O. Luzia, C.A.H. Laurindo, P.C. Soares, R.D. Torres, L.A. Mendes, F.L. Amorim, Recast layer mechanical properties of tool steel after electrical discharge machining with silicon powder in the dielectric, Int. J. Adv. Manuf. Technol. 103 (1–4) (2019) 15–28.

[26] S.O. Oparanti, I. Fofana, R. Jafari, R. Zarrougui, A state-of-the-art review on green nanofluids for transformer insulation, J. Mol. Liq. 396 (2024) 124023.
[27] J. Jiang, Z. Wu, S. Pan, X. Meng, D. Liu, K. Mu, et al., High-performance liquid metal-based SiC/graphene-Mo hybrid nanofluid for hydraulic transmission, Tribol. Int. 198 (2024) 109871.
[28] Y. Sun, R. Jiang, L. Hu, Y. Song, M. Li, Electrokinetic transport phenomena in nanofluidics and their applications, Electrophoresis 44 (17–18) (2023) 1756–1773.
[29] C. Rathnayaka, C.A. Amarasekara, K. Akabirov, M.C. Murphy, S. Park, M.A. Witek, et al., Nanofluidic devices for the separation of biomolecules, J. Chromatogr. A 1683 (2022) 463539.
[30] B. Mehta, D. Subhedar, H. Panchal, Z. Said, Synthesis, stability, thermophysical properties and heat transfer applications of nanofluid – a review, J. Mol. Liq. 364 (2022) 120034.
[31] C. Guo, X. Wang, W. Xie, S. Lai, Surface modification of aluminum alloy by wire electrical discharge machining with SiC nanofluid dielectric, Int. J. Adv. Manuf. Technol. 127 (7–8) (2023) 3525–3536.
[32] C. Guo, Z. Wu, X. Wang, J. Zhang, Comparison in performance by emulsion and SiC nanofluids HS-WEDM multi-cutting process, Int. J. Adv. Manuf. Technol. 116 (9–10) (2021) 3315–3324.